Draft version June 29, 2022
Typeset using LaTeX **twocolumn** style in AASTeX631

arXiv:2206.13525v1 [astro-ph.GA] 27 Jun 2022

Deep Spitzer/IRAC Data for $z \sim 10$ galaxies Reveal Blue Balmer Break Colors: Young Stellar Populations at ~ 500 Myr of Cosmic Time

Mauro Stefanon,[1,2,3,4] Rychard J. Bouwens,[4] Ivo Labbé,[5] Garth D. Illingworth,[6] Valentino Gonzalez,[7,8] and Pascal A. Oesch[9,10]

[1] *Departament d'Astronomia i Astrofisica, Universitat de València, C. Dr. Moliner 50, E-46100 Burjassot, València, Spain*
[2] *Observatori Astronòmic, Universitat de València, C/ Catedrático José Beltran, 2, 46980 Paterna València, Spain*
[3] *Unidad Asociada CSIC "Grupo de Astrofísica Extragaláctica y Cosmología" (Instituto de Física de Cantabria - Universitat de València)*
[4] *Leiden Observatory, Leiden University, NL-2300 RA Leiden, Netherlands*
[5] *Centre for Astrophysics and SuperComputing, Swinburne, University of Technology, Hawthorn, Victoria, 3122, Australia*
[6] *UCO/Lick Observatory, University of California, Santa Cruz, 1156 High St, Santa Cruz, CA 95064, USA*
[7] *Departamento de Astronomía, Universidad de Chile, Casilla 36-D, Santiago 7591245, Chile*
[8] *Centro de Astrofísica y Tecnologias Afines (CATA), Camino del Observatorio 1515, Las Condes, Santiago 7591245, Chile*
[9] *Departement d'Astronomie, Université de Genéve, 51 Ch. des Maillettes, CH-1290 Versoix, Switzerland*
[10] *Cosmic Dawn Center (DAWN), Niels Bohr Institute, University of Copenhagen, Jagtvej 128, København N, DK-2200, Denmark*

ABSTRACT

We present the deepest constraints yet on the median rest-UV+optical SED of $z \sim 10$ galaxies, prior to JWST science operations. We constructed stacks based on four robust J_{125}-dropouts, previously identified across the GOODS fields. We used archival HST/WFC3 data and the full depth Spitzer/IRAC mosaics from the GREATS program, the deepest coverage at $\sim 3-5\mu$m to date. The most remarkable feature of the SED is a blue IRAC $[3.6]-[4.5] = -0.18 \pm 0.25$ mag color. We also find a nearly flat $H_{160} - [3.6] = 0.07 \pm 0.22$ mag color, corresponding to a UV slope $\beta = -1.92 \pm 0.25$. This is consistent with previous studies, and indicative of minimal dust absorption. The observed blue IRAC color and SED fitting suggest that $z \sim 10$ galaxies have very young (few $\times$10 Myr) stellar populations, with 80% of stars being formed in the last $\lesssim 160$ Myr (2σ). While an exciting result, the uncertainties on the SED are too large to allow us to place strong constraints on the presence of a nebular continuum in $z \sim 10$ galaxies (as might be suggested by the blue $[3.6]-[4.5] < 0$ mag color). The resulting sSFR is consistent with the specific accretion rate of dark matter halos, indicative of a star-formation efficiency showing quite limited evolution at such early epochs.

Keywords: Primordial galaxies; High-redshift galaxies; Galaxy ages; Galaxy masses

1. INTRODUCTION

Understanding how efficiently stars formed out of the cold gas accreted through the potential wells of the hierarchical assembly of the dark matter halos is one of the most fundamental questions in modern astrophysics (e.g., Madau & Dickinson 2014).

Over the last decade, the sensitive and high spatial resolution data acquired by the Wide Field Camera 3 (WFC3) onboard the Hubble Space Telescope (HST) has enabled the detection and analysis of the rest-frame UV light emitted by recently-born massive O-B stars (e.g., Kennicutt 1998) up to $z \sim 10-12$ (Bouwens et al. 2013, Coe et al. 2013, Oesch et al. 2014, Bouwens et al. 2015, McLeod et al. 2016, Oesch et al. 2016, Calvi et al. 2016, Bernard et al. 2016, Oesch et al. 2018, Salmon et al. 2018, Ishigaki et al. 2018, Morishita et al. 2018, Bouwens et al. 2019, Lam et al. 2019, Salmon et al. 2020, Strait et al. 2020, Bouwens et al. 2022, Finkelstein et al. 2022 - see also Harikane et al. 2022 for $z \sim 12$ candidates identified from ground-based NIR data). These studies resulted in fundamental constraints to the total budget of newly-formed stars across $\gtrsim 13$ Gyr of lookback time (the so-called cosmic star-formation rate density - CSFRD - e.g., Bouwens et al. 2008, Oesch et al. 2014, Bouwens et al. 2015, Finkelstein et al. 2015b, Bouwens et al. 2016b, McLeod et al. 2016, Oesch et al. 2018, Ishi-

Email: mauro.stefanon@uv.es

gaki et al. 2018, Bhatawdekar et al. 2019, Bouwens et al. 2022).

Nonetheless, the highly successful Spitzer/IRAC camera (Fazio et al. 2004) has provided the community with an invaluable probe into the rest-frame optical light for galaxies at $z > 4$, complementing the information in the rest-frame UV from HST. These data have unveiled a very active Universe, where high equivalent widths EW ($> 500 - 1000$Å) line emission from the [O III]+Hβ (Labbé et al. 2013, Smit et al. 2014, Castellano et al. 2017, De Barros et al. 2019, Stefanon et al. 2019, Bowler et al. 2020, Strait et al. 2020, 2021, Endsley et al. 2021a, Stefanon et al. 2022b) and Hα (Smit et al. 2016, Bouwens et al. 2016a, Rasappu et al. 2016, Faisst et al. 2016, Mármol-Queraltó et al. 2016b, Caputi et al. 2017, Harikane et al. 2018, Lam et al. 2019, Faisst et al. 2019, Maseda et al. 2020, Stefanon et al. 2022a) are typical, and allowed to probe the stellar masses of galaxies at $z \sim 4-9$ (Duncan et al. 2014, Grazian et al. 2015, Song et al. 2016, Bhatawdekar et al. 2019, Kikuchihara et al. 2020), up to $z \sim 10$ (Oesch et al. 2016, Stefanon et al. 2021a).

The enormous progress in constraining the CSFRD and stellar mass, however, has not resulted yet in a clear consensus on the star-formation efficiency in the early Universe. For example, some studies report a $\sim 10\times$ higher abundance of galaxies at $6 < z < 10$ (e.g., Ellis et al. 2013, McLeod et al. 2016), and older stellar populations (Hashimoto et al. 2018, Roberts-Borsani et al. 2020, Mawatari et al. 2020, Tacchella et al. 2022), qualitatively consistent with a star-formation efficiency increasing with increasing redshifts at early epochs (e.g., Finkelstein et al. 2015a, Behroozi et al. 2019). However, a number of more recent determinations of the star-formation rate and stellar mass densities using the largest samples suggest that the baryonic assembly is consistent with the accretion of the dark matter halos (Oesch et al. 2018, Tacchella et al. 2018, Stefanon et al. 2021a). Clearly, JWST will rather quickly establish if the latest results are the most likely (or not!).

Interestingly, but perhaps not surprisingly, the current redshift frontier ($z \sim 9-12$) is where systematic differences in the stellar mass and stellar-to-halo mass ratio determinations are the most evident (see e.g., Stefanon et al. 2021a). Again, in this context, JWST observations will provide much more extensive insights, but we have the opportunity to make a significant step forward on this important question with existing data.

Observationally, the $M_\star/L$ ratio (where $M_\star$ indicates the stellar mass, and L the luminosity in a specific band), or, equivalently, the age of the stellar population, is arguably one of the main ingredients required to constrain the stellar mass assembly of galaxies. The Balmer/4000 Å break, one of the main proxies for stellar population age determinations (e.g., Kauffmann et al. 2003), is probed by the IRAC 3.6μm band for redshifts in the range $7.2 \lesssim z \lesssim 8.7$. At $z \sim 8.7$ the Balmer/4000Å break starts to leave the IRAC 3.6μm band, and by $z \sim 9.7$ it has completely shifted into the 4.5μm band. The 4.5μm band, instead, at $7.0 \lesssim z \lesssim 9.2$ intercepts the emission from the [O III]$_{\lambda\lambda 4959,5007}$ and Hβ lines, while for $z \gtrsim 9.2$ it is largely free of the most prominent emission lines (e.g., Anders & Fritze-v. Alvensleben 2003).

Fortunately, we can constrain the Balmer/4000Å break for $z \sim 10$ galaxies by leveraging Spitzer/IRAC observations. At these redshifts, the IRAC 3.6μm band probes the rest-frame UV ($\sim$ 3300Å rest-frame), while the 4.5μm band lies just red-ward of the Balmer/4000 Å break. This observational configuration is particularly effective at constraining the strength of the Balmer/4000Å break given the contiguity of the two IRAC bands. Moreover, at $z \lesssim 9$ the typical uncertainties in photometric redshifts ($\Delta z \sim 0.4$) can prevent from distinguishing genuine Balmer/4000 Å break from emission line contributing the 4.5μm band (see e.g., Figure 5 in Stefanon et al. 2021a), leading to potential overestimates of the stellar age (e.g., Stark et al. 2013, Stefanon et al. 2021a, Topping et al. 2022). Instead, the larger shift to redder wavelengths and the absence of strong line emission just red-ward of the Balmer break make this possibility less likely for $z \sim 10$ sources.

Thus, given the value of $z \sim 10$ samples for constraining the SFH, we focus on inferring the main stellar population parameters for a robust sample of star-forming galaxies at $z \sim 10$ (Oesch et al. 2018). In particular, we characterize the rest-frame optical light, complementing the previous study of Wilkins et al. (2016b) centered on the rest-frame UV light. We do so by stacking the very sensitive observations available with Spitzer/IRAC data over the GOODS fields (Giavalisco et al. 2004) from the GOODS Re-ionization Era wide Area Treasury from Spitzer (GREATS) + other programs (Stefanon et al. 2021b). GREATS combined all the relevant IRAC data (> 4200 hr cumulative in the 3.6 and 4.5μm bands) acquired throughout the scientific life of Spitzer, providing us with the deepest available $3-5\mu$m observations prior to the start of JWST science operations.

A brief description of the layout of this paper follows. In Section 2 we introduce the adopted sample and describe the relevant datasets, while in Section 3 we summarize our stacking procedure and the configurations we adopted to infer the main physical parameters. The resulting median spectral energy distribution (SED) is presented in Section 4, while in Section 5 we discuss its

Table 1. Sample of $z \sim 10$ star-forming galaxies adopted in this work.

ID	Redshift	$M_{\rm UV}$	5σ sensitivities[‡]	
			3.6μm	4.5μm
		(mag)	(nJy)	(nJy)
GN-z11	11.1 ± 0.1[*]	-21.6	53	78
GN-z10-2	9.9 ± 0.3	-20.7	67	103
GS-z10-1	9.9 ± 0.5	-20.6	51	79
XDFJ-3811362435	$9.9^{+0.7}_{-0.6}$	-17.6	48	77
Excluded[†]				
GN-z10-3[a]	8.78	-20.7	71	124
XDFJ-4023680031[b]	9.7 ± 0.6	-17.4	49	79

[*] Spectroscopic redshift from Oesch et al. (2018). Jiang et al. (2021) find a spectroscopic redshift of 10.957 ± 0.001 for this source.

[‡] Nominal 5σ sensitivities from the IRAC SENS-PET exposure time calculator adopting the coverage depths from the GREATS mosaics.

[†] Sources in the GOODS fields listed in Oesch et al. (2018) or Bouwens et al. (2015) but excluded from our analysis.

[a] This source appears as a bona-fide J-dropout in the selections of Oesch et al. (2014, 2018); however, given reports of Lyman-α emission from the source and its thus seeming to lie at $z = 8.78$ (Laporte et al. 2021), we exclude it from our stack results.

[b] Removed from our sample given the significant residuals present in the IRAC data after subtraction of the neighboring sources.

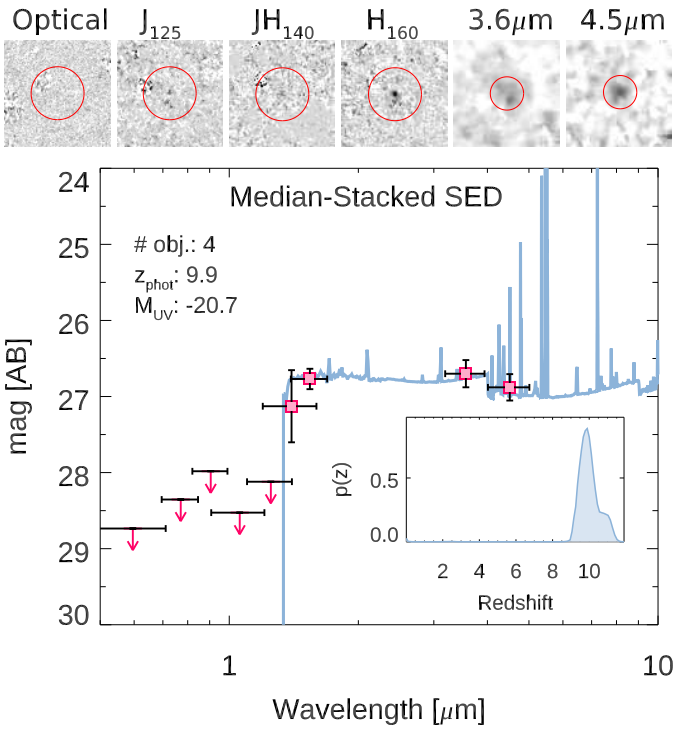


Figure 1. *Top panels:* Stacked image stamps in the *HST* and IRAC bands, as labelled at the top, centered on the median stacks. The stamps for the *HST* bands are 5.″0 per side, while those in the IRAC bands are 8.″0 wide. The *HST* optical stack combines all the data available blue-ward of the J_{125} band (i.e., $B_{435}, V_{606}, i_{775}$ and z_{850}). The red circle marks the 2.″5 diameter aperture adopted for our Spitzer/IRAC photometry. The *HST* stacks are shown for context, but we emphasise that our median *HST* flux measurements were derived from our photometry on individual sources. *Bottom panel:* Median-stacked SED resulting from our analysis. The stacked photometry is presented both as filled red squares with 1σ errors or as red downward-pointing arrows indicating 2σ upper limits. The effective width of each band is marked by the black horizontal bar. The blue curve corresponds to the best-fitting EAzY template. The inset shows the redshift probability distribution computed by EAzY. Labels at the top-left corner indicate the number of objects entering the stack, the median redshift, and the $M_{\rm UV}$ computed by EAzY (top to bottom, respectively). The SED is characterized by a blue IRAC $[3.6] - [4.5]$ color, indicative of young stellar populations.

implications in galaxy assembly in the early Universe. We summarize our findings in Section 6.

Throughout this paper, we adopt $\Omega_M = 0.3$, $\Omega_\Lambda = 0.7$ and $H_0 = 70\,{\rm km\ s^{-1}\ Mpc^{-1}}$, consistent with the most recent estimates from Planck (Planck Collaboration et al. 2020). Magnitudes are given in the AB system (Oke & Gunn 1983), while our $M_\star$ and SFR measurements are expressed in terms of the Salpeter (1955) initial mass function (IMF). For brevity, we denote the *HST* F435W, F606W, F775W, F850LP, F105W, F125W, F140W and F160W as B_{435}, V_{606}, i_{775}, z_{850}, Y_{105}, J_{125}, JH_{140} and H_{160}, respectively.

2. DATA

The initial $z \sim 10$ sample considered for this study is composed of the five candidate $z \sim 10$ Lyman-break galaxies identified as J_{125}-dropouts by Oesch et al. (2013, 2014, 2016, 2018), Bouwens et al. (2010, 2011a, 2015, 2016b) across the CANDELS (Grogin et al. 2011, Koekemoer et al. 2011) GOODS-N, GOODS-S (Giavalisco et al. 2004), the ERS field (Windhorst et al. 2011), and the UDF/XDF (Beckwith et al. 2006, Illingworth et al. 2013, Ellis et al. 2013) with the HUDF09-1 and HUFD09-2 parallels (Bouwens et al. 2011b). We complemented this sample with GN-z11 (Oesch et al. 2016), a star-forming galaxy spectroscopically confirmed

at $z_{\rm spec} = 11.1$ (Oesch et al. 2016 - see also Jiang et al. 2021). In Table 1 we list the sources considered for this study and the main properties of the imaging data sets. The HST mosaics are characterized by 5σ depths of ≈ 27.5 mag in the V_{606} and I_{814} bands, $\approx 26.7-27.5$ mag in the Y_{105}, and $\sim 26.8-27.8$ mag in the J_{125} and H_{160} bands. An essential aspect for our study is the availability of exquisitely-deep coverage at $3-5\mu$m in the GOODS fields from the Spitzer/IRAC GREATS program (PI: Labbé - Stefanon et al. 2021b). These mosaics combine all the useful IRAC imaging data acquired during the >15 years of Spitzer science operations, with typical 5σ depths of $\sim 26.0-27.0$ mag in the IRAC 3.6μm and 4.5μm bands.

Considering the typical uncertainties in photometric redshifts ($\Delta z \lesssim 0.6$), our $z\sim10$ sample selection minimizes the potential contamination of line emission which could affect the 4.5μm band for $z \lesssim 9$ sources (see e.g., Figure 5 of Stefanon et al. 2021a), increasing the robustness of the inferred physical properties.

To overcome the challenge posed by the broad Spitzer/IRAC PSF and light from neighbouring sources contaminating flux measurements at $>3\mu$m, we followed the procedure used in Stefanon et al. (2021a, 2022b) and Stefanon et al. (2022a) and subtracted the light from neighbouring sources with MOPHONGO (Labbé et al. 2006, 2010a,b, 2013, 2015). A critical ingredient for this step was the availability of accurate location-dependent PSFs from GREATS, as the asymmetric profile of the instrumental IRAC PSF and the variety of programs included in the mosaics result in significant variation of the PSF light profile across the mosaics (see e.g., Stefanon et al. 2021b). As a result of this process, one source (XDFJ-4023680031) was removed from our sample as it showed residual contamination after visual inspection.

Finally, we removed GN-z10-3 to be conservative. While it was initially identified at having a redshift of $z\sim10$ (Oesch et al. 2014), Laporte et al. (2021) report the detection of a candidate Lyα line, suggesting the redshift may be $z_{\rm Ly\alpha} = 8.78$ (Laporte et al. 2021). Our analysis therefore was conducted without GN-z10-3 and on the remaining four sources (see Table 1).

3. ANALYSIS

We applied our consolidated stacking procedure (Stefanon et al. 2022b,a for details) to construct the median spectral energy distribution (SED) of $z\sim10$ star-forming galaxies. We median-stacked the photometry in the HST bands normalized by the flux density in the H_{160} band of each source. Uncertainties associated with the flux densities were computed by bootstrapping the procedure 1000 times. The stacked flux density in the H_{160} band instead corresponds to the median of the individual photometric measurements, while the associated uncertainty was computed by bootstrapping the procedure 1000 times. For the IRAC 3.6μm and 4.5μm bands, instead, we median-stacked the image stamps centered on each source after normalizing them by the corresponding H_{160} flux density. For this step we combined the stamps obtained after removing the contribution of all neighbouring sources within a radius of $9\farcs0$. The flux density in the stacked IRAC stamps was measured in apertures of $2\farcs5$ diameter, and corrected to total flux densities using the median of the PSFs reconstructed at the location of each source (the applied correction factors are 1.85 and 1.91, for the 3.6 and 4.5μm band, respectively). Uncertainties were computed by measuring the dispersion of the flux density estimates in 20 $2\farcs5$-wide apertures randomly placed across the stacked stamp within $7.5''$ of the center, and repeating the process $10\times$ to increase the statistical significance. Finally, all values were rescaled by the median of the flux density in the H_{160} band. These stacked images then were used in our stellar population analysis.

We estimated the main stellar population parameters using the bayesian tool PROSPECTOR (Johnson et al. 2021), which runs on the FLEXIBLE STELLAR POPULATION SYNTHESIS (FSPS) package (Conroy & Wechsler 2009, Conroy & Gunn 2010) with the MODULES FOR EXPERIMENTS IN STELLAR ASTROPHYSICS ISOCHRONES AND STELLAR TRACKS (MIST; Choi et al. 2016, Dotter 2016). Our estimates are based on a Salpeter (1955) IMF defined between 0.1 and $240M_\odot$, a Calzetti et al. (2000) extinction curve, a $Z_{\rm star} \equiv Z_{\rm gas} = 0.2Z_\odot$ metallicity, a ionization parameter $\log U = -2.5$ (e.g., Stark et al. 2017, De Barros et al. 2019), and a formation redshift of $z=20$ (Mawatari et al. 2020, Hashimoto et al. 2018, Tacchella et al. 2022, Harikane et al. 2022).

Given that recent studies indicate that parametric star-formation histories (SFHs) could be underestimating the masses at high redshifts (e.g., Leja et al. 2019b, Topping et al. 2022), we considered two different star formation histories: a constant (CSFH), and a non-parametric SFH. In particular, we assumed that the non-parametric SFH was defined by four bins in lookback time, which we fixed at $0-3$Myr, $3-13$Myr, $13-100$ Myr, and $100-300$ Myr, respectively, with a Student's t-distribution continuity prior modulating the ratio of the SFR in contiguous bins, with $\nu=2$ and $\sigma=2$ (see discussions in Leja et al. 2019a, Tacchella et al. 2022). This configuration can concurrently accommodate a recent burst of star formation and significant star formation

during the initial assembly of the galaxy (Hashimoto et al. 2018, Roberts-Borsani et al. 2020, Tacchella et al. 2022). We also repeated the process with up to 8 bins in lookback time ($0-3$Myr, $3-13$Myr, $13-100$ Myr, and log-spaced at later lookback times) and found similar results.

Finally, we also considered a third model with a constant SFH and pure stellar emission (i.e., assuming the nebular continuum and line emission are negligible). During the fits, the redshift was fixed to the median of the photometric redshifts of the sample ($z_{\rm median}$). Instead, the SFR integrated over the cosmic time (i.e, the total mass $M_{\rm T}$) and the dust optical depth at 5500Å (τ_{5500}) varied under a flat prior ($6 \leq \log M_{\rm T}/M_{\odot} \leq 11$ and $0 \leq \tau_{5500} \leq 5$, respectively). Nonetheless, the mass values quoted in this paper refer to the mass in surviving stars (i.e, stellar mass $M_{\star}$), obtained by rescaling $M_{\rm T}$ by the estimated stellar-to-total mass ratio (the MFRAC parameter, with typical values in the range $\sim 0.8-1.0$).

SFR were computed by converting the UV luminosity using the factors listed by Madau & Dickinson (2014), interpolated for a $Z = 0.2Z_{\odot}$ metallicity and a Salpeter (1955) IMF. Because of the increasing indication of negligible dust emission at early epochs (e.g., Bouwens et al. 2016b, Dunlop et al. 2017, McLure et al. 2018, Bouwens et al. 2020), and considering the small A_V values obtained with the non-parametric and CSFH configurations (see Section 5), we opted for not correcting the SFR for dust extinction. We finally computed the sSFR ($\equiv$SFR$/M_{\star}$) combining the SFR and $M_{\star}$ values previously estimated.

4. RESULTS

Table 2 lists the photometric measurements from our stacking procedure, while in Figure 1 we display the stacked stamps and the measured broad-band SED. To further validate our stacking analysis, and as an initial guide to the interpretation of our results, in Figure 1 we also present the best-fitting template from EAzY (Brammer et al. 2008 - see Stefanon et al. 2021a, 2022b for details on the template set we adopted with EAzY).

The most prominent feature consists of a blue $[3.6]-[4.5] = -0.18 \pm 0.25$ mag color. Because at $z \sim 10$ the IRAC 3.6μm band probes the rest-UV, while the 4.5μm band lies just red-ward of the Balmer/4000Å break, the $[3.6]-[4.5]$ color brackets the Balmer/4000Å break, an indicator of stellar population age (e.g., Kauffmann et al. 2003). The measured blue color then suggests young stellar populations (e.g., Inoue 2011), either as the result of a very rapid assembly of stars (e.g., an exponentially rising SFH) or as a recent burst of star formation. We will return to the implications of the $[3.6]-[4.5]$ color on the stellar populations at $z \sim 10$ in Section 5.1.

Our stacked SED is also characterized by an approximately flat $H_{160}-[3.6] = 0.07 \pm 0.22$ mag color, corresponding to a UV slope $\beta = -1.92 \pm 0.25$, marginally redder than, but consistent with, the previous estimates of $\beta = -2.1 \pm 0.3$ at $z \sim 10$ by Wilkins et al. (2016a). This result is not very surprising, considering that 3/4 of the sources in our sample are in common with that of Wilkins et al. (2016a). Our UV slope estimate is also consistent with the recent measurements for $z \sim 9$ sources by Bhatawdekar & Conselice (2021, $\beta = -2.1 \pm 0.4$ for $M_{\rm UV} \sim -21$ mag) and Tacchella et al. (2022, $\beta = -1.9 \pm 0.3$). It is reassuring to find consistent measurements, considering the IRAC data adopted for this work (Stefanon et al. 2021b) have on average $\sim 2\times$ longer exposure times than the mosaics available to Wilkins et al. (2016a).

5. DISCUSSION

Figure 2 displays the results of our template fitting analysis, while in Table 3 we list the the values of the main physical parameters. In what follows, we adopt the results from the non-parametric SFH as reference.

5.1. *Which are the typical stellar population ages at ~ 500 Myr of cosmic time?*

Interestingly, inspection of the non-parametric SFH shows that $\sim 62\%$ of the stellar mass is created in a burst during the most recent 3 Myr, a fraction that only marginally ($< 0.5\%$) depends on the number of lookback time bins adopted as a prior for the SFH (see Section 3). However, it also indicates that 80% of stars were formed in the last $\lesssim 160$ Myr (2σ), suggesting that sustained star formation could be happening at earlier phases of mass assembly.

The analysis assuming a constant SFH and nebular emission results in an extremely young stellar population age, $\log(\text{age/yr}) = 6.7^{+0.6}_{-0.4}$. Remarkably, the corresponding best fit SED and main stellar population parameters are very close ($\Delta \log M_{\star} \sim 0.08$dex, $\Delta A_V \sim 0.02$ mag) to those obtained with the non-parametric SFH, increasing the overall confidence on this result. Interestingly, the M_T for the non-parametric SFH is ~ 0.2 dex larger than that for the CSFH, consistent with recent results (e.g., Tacchella et al. 2022). Indeed, we find a ~ 1 dex larger value of $\log(t_{\ell,80}/\text{yr})$ for the non-parametric SFH, consistent with a scenario of considerable star formation at the beginning of mass

Table 2. Flux densities for our median-stacked photometry

	V_{606} (nJy)	i_{775} (nJy)	z_{850} (nJy)	Y_{105} (nJy)	J_{125} (nJy)	JH_{140} (nJy)	H_{160} (nJy)	3.6μm (nJy)	4.5μm (nJy)
Stack	-1.0 ± 5.8	-0.6 ± 8.3	-5.1 ± 11.6	-4.7 ± 7.1	14.7 ± 10.3	51.2 ± 22.3	71.2 ± 8.8	75.8 ± 12.5	64.3 ± 10.3

NOTE—We only list the flux densities in those bands available for at least 90% of the sources in our sample.

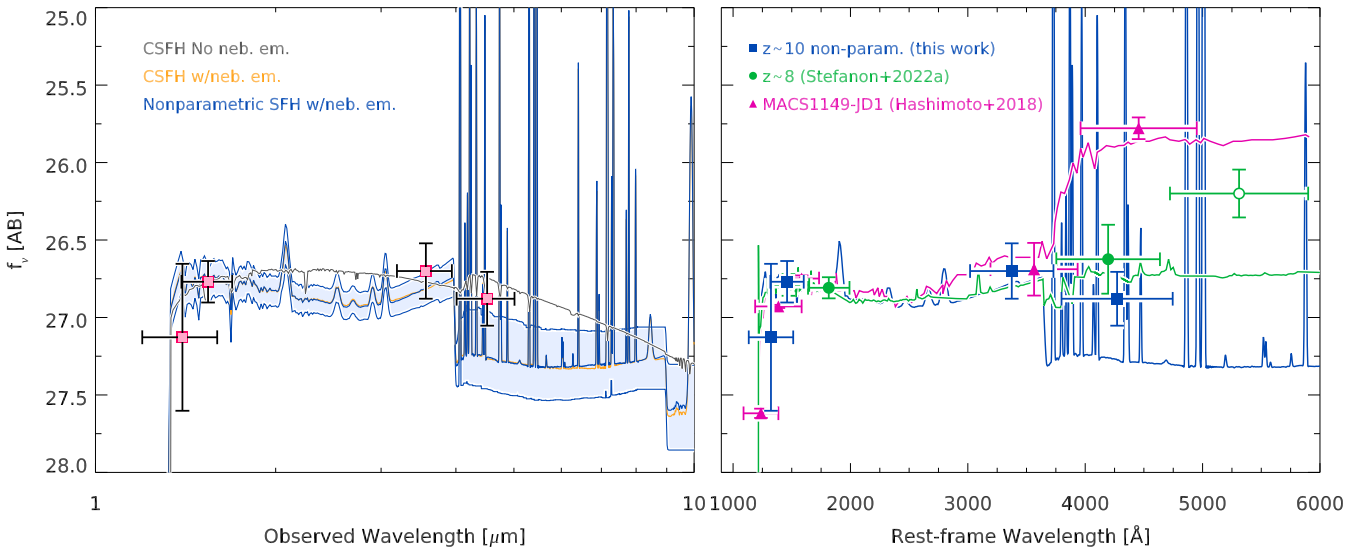


Figure 2. [*Left*] Best-fit SEDs resulting from the different configurations adopted in estimating the main stellar population parameters of our stack. In particular, we considered a constant SFH (CSFH) model with and without nebular emission (orange and grey solid curves, respectively), and a non-parametric SFH (blue curve - see Section 3 for details), which we adopt as reference (the orange and blue curves are essentially indistinguishable). The filled blue area corresponds to the SED posteriors marginalized over the 68% confidence interval for the non-parametric configuration. [*Right*] Comparison of our SED at $z \sim 10$ (filled blue squares and curve) with results from other studies. Specifically, we show the median SED at $z \sim 8$ corresponding to the $M_{\rm UV} \sim -20.7$ mag bin from Stefanon et al. (2022b, green circles and curve), and the SED of MACS1149-JD1 (Hashimoto et al. 2018, filled purple triangles and curve - here we adopt the photometric measurements of Zheng et al. 2017), a star-forming galaxy at $z_{\rm spec} = 9.1$ characterized by an apparent, pronounced Balmer break (Hashimoto et al. 2018). All wavelengths have been shifted to their rest frame. The photometric measurements and best-fit SEDs from Stefanon et al. (2022b), Hashimoto et al. (2018) and Zheng et al. (2017) have been renormalized to match the luminosity of our $z \sim 10$ stack at 1600Å. We removed the main emission lines from the SEDs of Stefanon et al. (2022b) and Hashimoto et al. (2018) to improve readability, but note the likely substantial contribution of the [O III]$_{\lambda\lambda 4959,5007}$ doublet to the measured flux at $\lambda \sim 5200$Å for the Stefanon et al. (2022b) results (open green circle). Our stacked photometry can be better described by young stellar population templates, a result likely driven by the observed blue $[3.6]-[4.5] \lesssim 0$ mag color, consistent with the previous median determinations at $z \sim 8$ by Stefanon et al. (2022b).

assembly. Instead, different MFRAC values (0.78 and 1.0 for the non-parametric and CSFH, respectively) mitigate the 0.2 dex systematic difference, leading to similar $M_\star$ estimates.

The measured blue $[3.6]-[4.5] \lesssim 0$ mag color might be seen as suggestive of a Balmer jump SED, seen in very young stellar populations (e.g., Bica et al. 1994, Inoue 2011, Schaerer & de Barros 2009, 2010). However, the $[3.6]-[4.5] < 0$ mag color isn't even significant at 1σ, and the result can also be fit (reduced $\chi^2 \sim 0.6$) by a very young stellar population ($\sim 10^{6.4}$ yr) with no nebular continuum and a modest amount of dust extinction ($A_V \sim 1.1$ mag, leading to a ~ 1 dex larger stellar mass).

ALMA results also provide additional insights in this context. The obscured SFR for XDFJ-3811362435 corresponding to $A_V = 1.1$ mag is $\rm SFR_{obscured} \approx$

Table 3. Main stellar population parameters inferred for our stacked SED

Property	Value		
$z_{\rm median}$	9.9		
$M_{\rm UV}$	-20.7 ± 0.1 mag		
UV slope β	-1.92 ± 0.25		
$\rm SFR_{UV}$ †	$9.1^{+0.9}_{-0.8} M_\odot$/yr		
SFH	Non Param.	CSFH	CSFH no neb.
$\log(t_{\ell,50}/{\rm yr})$ ‡	$6.4^{+1.2}_{-0.2}$	$6.4^{+0.7}_{-0.4}$	$6.1^{+0.2}_{-0.4}$
$\log(t_{\ell,80}/{\rm yr})$ ‡	$7.6^{+0.6}_{-1.2}$	$6.6^{+0.7}_{-0.4}$	$6.3^{+0.2}_{-0.4}$
$\log(M_\star/M_\odot)$	$8.4^{+0.4}_{-0.2}$	$8.4^{+0.3}_{-0.1}$	$9.3^{+0.1}_{-0.4}$
A_V/mag	$0.2^{+0.1}_{-0.1}$	$0.2^{+0.1}_{-0.1}$	$1.1^{+1.1}_{-0.6}$
sSFR/$\rm Gyr^{-1}$ *	$33.4^{+24.1}_{-19.8}$	$40.0^{+27.5}_{-36.0}$	$4.6^{+5.9}_{-0.7}$ ♪

NOTE—The measurements for $\log(t_{\ell,50}/{\rm yr})$, $\log(t_{\ell,80}/{\rm yr})$, $\log(M_\star/M_\odot)$, A_V and sSFR refer to the median and $16-84$ percentiles of the posteriors.

† SFR computed from the rest-frame UV luminosity and assuming negligible dust obscuration. We warn the reader that, given the high fraction of obscured star formation in the configuration without nebular emission (CSFH no neb.), the corresponding $\rm SFR_{UV}$ value is potentially underestimated. Assuming a Calzetti et al. (2000) curve, the unobscured+obscured SFR for this configuration would result in a $\approx 12\times$ larger value. This however is not the option that we consider to be most likely.

‡ Look-back time encapsulating 50% and 80% ($\log(t_{\ell,50}/{\rm yr})$ and $\log(t_{\ell,80}/{\rm yr})$, respectively) of stellar mass assembly.

* sSFR obtained dividing the unobscured $\rm SFR_{UV}$ by the stellar mass $M_\star$.

♪ This value of sSFR does not account for the obscured fraction of SFR, and it is therefore likely underestimated in this case. A correction assuming a Calzetti et al. (2000) extinction curve would result in a $\approx 12\times$ larger value. Again this is not the option that we consider to be the most likely.

$6 M_\odot$ $\rm yr^{-1}$[1], significantly below the 4σ threshold ($\sim 51 M_\odot {\rm yr}^{-1}$ e.g., Bouwens et al. 2020, after conversion to a Salpeter 1955 IMF) in the deep ALMA continuum mapping of the XDF region (ASPECS: Walter et al. 2016, Decarli et al. 2019; see also Dunlop et al. 2017).

[1] We assumed the IRX-β relation (where IRX$\equiv L_{\rm IR}/L_{\rm UV}$ is the infrared excess, with $L_{\rm IR}$ and $L_{\rm UV}$ the infrared and UV luminosities, respectively - e.g., Meurer et al. 1999) for a Calzetti et al. (2000) attenuation curve. This relationship was shifted to match an unattenuated $\beta = -3$, consistent with the intrinsic UV slope of the unattenuated best-fit SED template, resulting in IRX$\sim$ 10 for $\beta = -3$. The SFR corresponding to $L_{\rm IR}$ was estimated adopting the Kennicutt (1998) conversion.)

This results in no effective help in removing the degeneracy between the different SED solutions. Similarly, the $\rm SFR_{obscured} \approx 90 M_\odot$ $\rm yr^{-1}$ for the median SED lies below the detection threshold ($\approx 700 M_\odot$ $\rm yr^{-1}$ at 4σ) of the wide-area coverage of GOODS-ALMA (Franco et al. 2018), suggesting that sensitivities similar to ASPECS would be required to ascertain the existence of brighter (but rarer) dusty sources. An even shallower coverage exists in the FIR for GOODS-N (e.g., Dowell et al. 2014, Liu et al. 2018), limiting further considerations. Instead, and qualitatively, the strong [O III]+Hβ line emission in star-forming galaxies (equivalent width EW$\gtrsim$ 500 − 1000Å) at $6 \lesssim z \lesssim 8$ (see Section 1 for references) supports a similar scenario with significant nebular continuum at $z \sim 10$, just ~ 150 Myr earlier than $z \sim 8$, consistent with both the non-parametric and CSFH configurations.

5.2. *Comparison to previous studies*

Our results are consistent with the average blue color and young stellar ages Stefanon et al. (2022b) found for star-forming galaxies at $z \sim 8$, and with recent analyses of individual sources in samples at $z > 7$ (e.g., Strait et al. 2020, Topping et al. 2022). Nonetheless, indication of red IRAC $[3.6]-[4.5] > 0$ mag colors, suggestive of the presence of a Balmer break and more evolved stellar populations, have been found for *some* individual sources at similar redshifts (e.g., Roberts-Borsani et al. 2016, Huang et al. 2016, Hashimoto et al. 2018, Strait et al. 2020, Laporte et al. 2021, Tacchella et al. 2022, Roberts-Borsani et al. 2022).

One potential limitation of current results at $z \sim 9$ consists in the small number of sources with spectroscopic confirmation (only four galaxies with $8.5 \leq z_{\rm spec} \leq 9.5$ exist in the literature: Zitrin et al. 2015, Hashimoto et al. 2018, Laporte et al. 2021, Larson et al. 2022). The typical uncertainties from photometric redshifts at $z \sim 9$ generally do not enable us to ascertain whether the IRAC 4.5μm band is probing exclusively the stellar+nebular continuum or if instead it is also intercepting the contribution from strong emission by [O III]+Hβ, making the interpretation of red $[3.6]-[4.5] > 0$ mag colors more uncertain.

Nonetheless, recent works have shown the existence of sources with $z_{\rm spec} \gtrsim 9$ and red IRAC colors (Hashimoto et al. 2018, Laporte et al. 2021). MACS1149-JD1 (Zheng et al. 2012, Hoag et al. 2018, Hashimoto et al. 2018), at $z_{\rm spec} = 9.1$ (Hashimoto et al. 2018), is perhaps the most enigmatic representative of this category. Its exceptionally red $[3.6]-[4.5] \sim 0.9$ mag color, indicative of a pronounced Balmer break, clearly contrasts with the $\sim$ blue $[3.6]-[4.5] \lesssim 0$ mag color we find in our

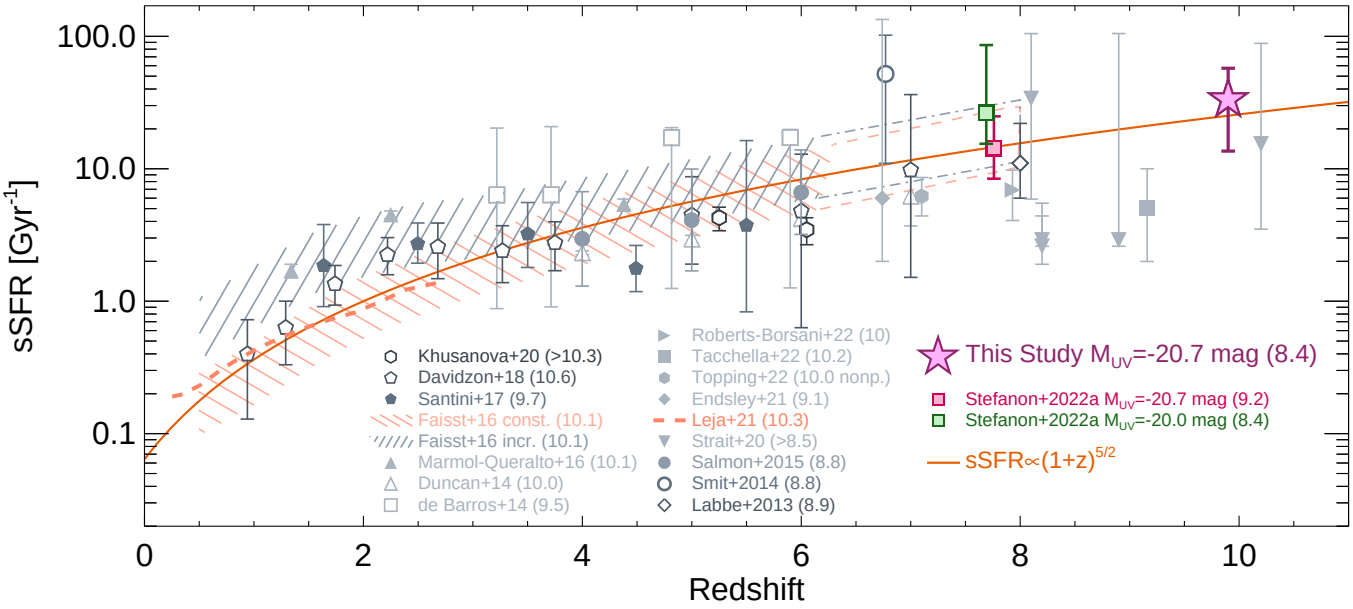


Figure 3. Evolution of the sSFR since $z \sim 10$. The estimate from this work (filled purple star) is presented together with determinations from the literature indicated by the legend. The number in parenthesis indicates the $\log M_\star$ for each set of measurement, converted to a Salpeter (1955) IMF whenever necessary following the prescription of Madau & Dickinson (2014). The solid orange curve corresponds to the sSFR predicted by the strikingly simple model of Dekel et al. (2013), which builds on the assumption that the formation of stars in galaxies is dominated by the inflow of cold gas driven by the hierarchical merging of the dark matter halos. Our new measurement at $z \sim 10$ is consistent with the model prediction, suggesting marginal evolution in the star-formation efficiency of galaxies with cosmic time. This supports previous findings at $z \sim 8$ (e.g., Stefanon et al. 2022b), and is indicative of minimal evolution in the star formation efficiency with cosmic time, beginning as early as just ~ 500 Myr after the Big Bang.

study (see Figure 2). It is also worth noting that while spectroscopic redshifts are necessary to accurately establishing which emission lines could be contributing to the flux densities in IRAC bands, they are not always sufficient to robustly segregate evolved from young stellar population ages for $z \lesssim 9$ sources (e.g., GN-z10-3, see Laporte et al. 2021 and Figure 2 of Topping et al. 2022). The medium-band JWST/NIRCam filters and JWST/NIRSpec observations will soon enable to probe the rest-frame optical continuum in between the emission lines at high-z, providing key information to explore the ages and star-formation histories of the earliest generations of galaxies.

5.3. *Evolution of the sSFR*

The value we obtained for the sSFR is displayed in Figure 3 together with previous determinations from the literature at $1 \lesssim z \lesssim 10$ (Labbé et al. 2013, Smit et al. 2014, Duncan et al. 2014, Salmon et al. 2015, Mármol-Queraltó et al. 2016a, Santini et al. 2017, Davidzon et al. 2018, Khusanova et al. 2020, Strait et al. 2020, Endsley et al. 2021b, Faisst et al. 2016, Leja et al. 2021, Topping et al. 2022, Tacchella et al. 2022, Roberts-Borsani et al. 2022).

Our new determination is consistent with the measurements of Stefanon et al. (2022b) and Labbé et al. (2013) at $z \sim 8$, and at $\lesssim 2\sigma$ with those of Strait et al. (2020) at $z \gtrsim 8$ and with the median for a sample at $z \sim 9$ analized by Tacchella et al. (2022). Comparison of these measurements to those at lower redshifts suggests a sSFR monotonically growing with increasing redshift up to $z \sim 10$, albeit with a large ≈ 1 dex scatter.

Finally, to gather insights into the relationship between the hierarchical assembly of the dark matter halos and the stellar mass accretion of galaxies, in Figure 3 we also compare the measurements to the evolution of the sSFR predicted by Dekel et al. (2013). This was obtained through analytical considerations on the Extended Press-Schechter formalism which describes the assembly rate of the dark matter halos (see also Neistein & Dekel 2008, Weinmann et al. 2011, Genel et al. 2014). The final values for the sSFR were obtained assuming that the baryonic accretion involved exclusively cold gas, corresponding to a time-independent conversion factor between the specific accretion rate of the dark matter halos and the sSFR. The agreement between our $z \sim 10$ estimate and the model prediction is quite remarkable, considering the minimal set of assumptions

adopted in Dekel et al. (2013) model.

Stefanon et al. (2022b) found that galaxy assembly in the early Universe was dominated by the accretion of dark matter halos and cold gas, with minimal evolution in the star formation efficiency (SFE). The determination of the sSFR to $z \sim 10$ from the present study extends that earlier result of an unevolving SFE by ~ 150 Myr to just $\sim$ 500 Myr of cosmic time. In particular, this result qualitatively supports the non-evolving stellar-to-halo mass ratio at $4 \lesssim z \lesssim 10$ inferred by Stefanon et al. (2021a) from the analysis of the stellar mass function of star-forming galaxies. This built on the work of Stefanon et al. 2017 using the evolution of the rest-frame optical luminosity function, and of Bouwens et al. (2015, 2021) based on the evolution in the UV LF from $z \sim 10$ to $z \sim 0$. Interestingly, this is consistent with predictions of recent models (e.g., Tacchella et al. 2018, Park et al. 2019).

6. CONCLUSIONS

We derive the median SED of star-forming galaxies at $z \sim 10$, obtained by stacking the Spitzer/IRAC 3.6 and 4.5μm image stamps, and the *HST* photometry, of four robust J_{125} dropouts previously identified over the GOODS fields.

Crucial for our study are the deepest data at $3-5\mu$m before JWST starts its operations, provided by the GREATS program (PI: Labbé - Stefanon et al. 2021b), which at these redshifts bracket the Balmer/4000Å break, a proxy for the age of the stellar population.

The most fascinating feature seen in the stacked SED is a blue $[3.6]-[4.5] = -0.18 \pm 0.25$ mag color. At these redshifts, the 3.6μm band probes the rest-frame UV, while the 4.5μm band intercepts the rest-frame optical light. Given the wavelength contiguity of these two bands, the observed blue IRAC color suggests very young stellar populations. Indeed, a quantitative analysis through SED template fitting performed with PROSPECTOR (Leja et al. 2019a, Johnson et al. 2021) indicates that 80% of the stars assembled in the most recent $\lesssim$ 160 Myr (2σ). The observed blue color contrasts with the red $[3.6]-[4.5]$ measurements for some sources in recent studies (e.g., MACS1149-JD1 - Hashimoto et al. 2018).

Finally, using the results from the SED fitting, we compute the sSFR. Our value is generally consistent with previous determinations at $z \lesssim 9$, although some estimates form the literature are only consistent at $\sim 2\sigma$. Overall, our analysis confirms the trend for a monotonic increase of the sSFR with increasing redshifts, previously found for $z \lesssim 8$ (e.g., Faisst et al. 2016, Stefanon et al. 2022b). The sSFR measurements for $3 \lesssim z \lesssim 10$ are also broadly consistent with the toy-model of Dekel et al. (2013), in which the formation of stars is dominated by the inflow of cold gas driven by the hierarchical merging of the dark matter halos.

This result, at $z \sim 10$, corresponding to just $\sim$ 500 Myr of cosmic time, extends earlier results at $z \sim 8$ by Stefanon et al. (2022b), and indicates that galaxy assembly in the early Universe was dominated by the accretion of dark matter halos and cold gas, with minimal evolution in the star formation efficiency (SFE).

Clearly, JWST science operations will provide completely game-changing insights into the stellar populations of galaxies and their prevalence earlier than 500 Myr of cosmic time thanks to the exquisite capabilities of JWST/NIRSpec, NIRCam and MIRI, facilitating a major leap in our understanding of galaxy formation. Our Hubble/Spitzer driven result hints at exciting future insights from JWST's study of the earliest galaxies.

MS acknowledges support from the CIDEGENT grant CIDEGENT/2021/059. MS and RJB acknowledge support from TOP grant TOP1.16.057. PAO acknowledges support from the Swiss National Science Foundation through the SNSF Professorship grant 190079 'Galaxy Build-up at Cosmic Dawn'. The Cosmic Dawn Center (DAWN) is funded by the Danish National Research Foundation under grant No. 140. We also acknowledge the support of NASA grants HSTAR-13252, HST-GO-13872, HST-GO-13792, and NWO grant 600.065.140.11N211 (vrij competitie). GDI acknowledges support for GREATS under RSA No. 1525754. This paper utilizes observations obtained with the NASA/ESA *Hubble Space Telescope*, retrieved from the Mikulski Archive for Space Telescopes (MAST) at the Space Telescope Science Institute (STScI). STScI is operated by the Association of Universities for Research in Astronomy, Inc. under NASA contract NAS 5-26555. This work is based [in part] on observations made with the *Spitzer Space Telescope*, which was operated by the Jet Propulsion Laboratory, California Institute of Technology under a contract with NASA. Support for this work was provided by NASA through an award issued by JPL/Caltech.

REFERENCES

Anders, P., & Fritze-v. Alvensleben, U. 2003, A&A, 401, 1063

Beckwith, S. V. W., Stiavelli, M., Koekemoer, A. M., et al. 2006, AJ, 132, 1729

Behroozi, P., Wechsler, R. H., Hearin, A. P., & Conroy, C. 2019, MNRAS, 488, 3143
Bernard, S. R., Carrasco, D., Trenti, M., et al. 2016, ApJ, 827, 76
Bhatawdekar, R., & Conselice, C. J. 2021, ApJ, 909, 144
Bhatawdekar, R., Conselice, C. J., Margalef-Bentabol, B., & Duncan, K. 2019, MNRAS, 486, 3805
Bica, E., Alloin, D., & Schmitt, H. R. 1994, A&A, 283, 805
Bouwens, R., González-López, J., Aravena, M., et al. 2020, ApJ, 902, 112
Bouwens, R. J., Illingworth, G. D., Franx, M., & Ford, H. 2008, ApJ, 686, 230
Bouwens, R. J., Illingworth, G. D., van Dokkum, P. G., et al. 2022, ApJ, 927, 81
Bouwens, R. J., Smit, R., Labbé, I., et al. 2016a, ApJ, 831, 176
Bouwens, R. J., Stefanon, M., Oesch, P. A., et al. 2019, ApJ, 880, 25
Bouwens, R. J., Illingworth, G. D., González, V., et al. 2010, ApJ, 725, 1587
Bouwens, R. J., Illingworth, G. D., Labbe, I., et al. 2011a, Nature, 469, 504
Bouwens, R. J., Illingworth, G. D., Oesch, P. A., et al. 2011b, ApJ, 737, 90
Bouwens, R. J., Oesch, P. A., Illingworth, G. D., et al. 2013, ApJL, 765, L16
Bouwens, R. J., Illingworth, G. D., Oesch, P. A., et al. 2015, ApJ, 803, 34
Bouwens, R. J., Oesch, P. A., Labbé, I., et al. 2016b, ApJ, 830, 67
Bouwens, R. J., Oesch, P. A., Stefanon, M., et al. 2021, AJ, 162, 47
Bowler, R. A. A., Jarvis, M. J., Dunlop, J. S., et al. 2020, MNRAS, 493, 2059
Brammer, G. B., van Dokkum, P. G., & Coppi, P. 2008, ApJ, 686, 1503
Calvi, V., Trenti, M., Stiavelli, M., et al. 2016, ApJ, 817, 120
Calzetti, D., Armus, L., Bohlin, R. C., et al. 2000, ApJ, 533, 682
Caputi, K. I., Deshmukh, S., Ashby, M. L. N., et al. 2017, ApJ, 849, 45
Castellano, M., Pentericci, L., Fontana, A., et al. 2017, ApJ, 839, 73
Choi, J., Dotter, A., Conroy, C., et al. 2016, ApJ, 823, 102
Coe, D., Zitrin, A., Carrasco, M., et al. 2013, ApJ, 762, 32
Conroy, C., & Gunn, J. E. 2010, ApJ, 712, 833
Conroy, C., & Wechsler, R. H. 2009, ApJ, 696, 620
Davidzon, I., Ilbert, O., Faisst, A. L., Sparre, M., & Capak, P. L. 2018, ApJ, 852, 107
De Barros, S., Oesch, P. A., Labbé, I., et al. 2019, MNRAS, 489, 2355
Decarli, R., Walter, F., Gónzalez-López, J., et al. 2019, ApJ, 882, 138
Dekel, A., Zolotov, A., Tweed, D., et al. 2013, MNRAS, 435, 999
Dotter, A. 2016, ApJS, 222, 8
Dowell, C. D., Conley, A., Glenn, J., et al. 2014, ApJ, 780, 75
Duncan, K., Conselice, C. J., Mortlock, A., et al. 2014, MNRAS, 444, 2960
Dunlop, J. S., McLure, R. J., Biggs, A. D., et al. 2017, MNRAS, 466, 861
Ellis, R. S., McLure, R. J., Dunlop, J. S., et al. 2013, ApJL, 763, L7
Endsley, R., Stark, D. P., Charlot, S., et al. 2021a, MNRAS, 502, 6044
Endsley, R., Stark, D. P., Chevallard, J., & Charlot, S. 2021b, MNRAS, 500, 5229
Faisst, A. L., Capak, P. L., Emami, N., Tacchella, S., & Larson, K. L. 2019, ApJ, 884, 133
Faisst, A. L., Capak, P., Hsieh, B. C., et al. 2016, ApJ, 821, 122
Fazio, G. G., Hora, J. L., Allen, L. E., et al. 2004, ApJS, 154, 10
Finkelstein, S. L., Song, M., Behroozi, P., et al. 2015a, ApJ, 814, 95
Finkelstein, S. L., Ryan, Jr., R. E., Papovich, C., et al. 2015b, ApJ, 810, 71
Finkelstein, S. L., Bagley, M., Song, M., et al. 2022, ApJ, 928, 52
Franco, M., Elbaz, D., Béthermin, M., et al. 2018, A&A, 620, A152
Genel, S., Vogelsberger, M., Springel, V., et al. 2014, MNRAS, 445, 175
Giavalisco, M., Ferguson, H. C., Koekemoer, A. M., et al. 2004, ApJL, 600, L93
Grazian, A., Fontana, A., Santini, P., et al. 2015, A&A, 575, A96
Grogin, N. A., Kocevski, D. D., Faber, S. M., et al. 2011, ApJS, 197, 35
Harikane, Y., Ouchi, M., Shibuya, T., et al. 2018, ApJ, 859, 84
Harikane, Y., Ono, Y., Ouchi, M., et al. 2022, ApJS, 259, 20
Hashimoto, T., Laporte, N., Mawatari, K., et al. 2018, Nature, 557, 392
Hoag, A., Bradač, M., Brammer, G., et al. 2018, ApJ, 854, 39
Huang, K.-H., Lemaux, B. C., Schmidt, K. B., et al. 2016, ApJL, 823, L14

Illingworth, G. D., Magee, D., Oesch, P. A., et al. 2013, ApJS, 209, 6
Inoue, A. K. 2011, MNRAS, 415, 2920
Ishigaki, M., Kawamata, R., Ouchi, M., et al. 2018, ApJ, 854, 73
Jiang, L., Kashikawa, N., Wang, S., et al. 2021, Nature Astronomy, 5, 256
Johnson, B. D., Leja, J., Conroy, C., & Speagle, J. S. 2021, ApJS, 254, 22
Kauffmann, G., Heckman, T. M., White, S. D. M., et al. 2003, MNRAS, 341, 33
Kennicutt, Jr., R. C. 1998, ARA&A, 36, 189
Khusanova, Y., Béthermin, M., Le Fèvre, O., et al. 2020, arXiv e-prints, arXiv:2007.08384
Kikuchihara, S., Ouchi, M., Ono, Y., et al. 2020, ApJ, 893, 60
Koekemoer, A. M., Faber, S. M., Ferguson, H. C., et al. 2011, ApJS, 197, 36
Labbé, I., Bouwens, R., Illingworth, G. D., & Franx, M. 2006, ApJL, 649, L67
Labbé, I., González, V., Bouwens, R. J., et al. 2010a, ApJL, 716, L103
—. 2010b, ApJL, 708, L26
Labbé, I., Oesch, P. A., Bouwens, R. J., et al. 2013, ApJL, 777, L19
Labbé, I., Oesch, P. A., Illingworth, G. D., et al. 2015, ApJS, 221, 23
Lam, D., Bouwens, R. J., Labbé, I., et al. 2019, A&A, 627, A164
Laporte, N., Meyer, R. A., Ellis, R. S., et al. 2021, MNRAS, 505, 3336
Larson, R. L., Finkelstein, S. L., Hutchison, T. A., et al. 2022, arXiv e-prints, arXiv:2203.08461
Leja, J., Carnall, A. C., Johnson, B. D., Conroy, C., & Speagle, J. S. 2019a, ApJ, 876, 3
Leja, J., Johnson, B. D., Conroy, C., et al. 2019b, ApJ, 877, 140
Leja, J., Speagle, J. S., Ting, Y.-S., et al. 2021, arXiv e-prints, arXiv:2110.04314
Liu, D., Daddi, E., Dickinson, M., et al. 2018, ApJ, 853, 172
Madau, P., & Dickinson, M. 2014, ARA&A, 52, 415
Mármol-Queraltó, E., McLure, R. J., Cullen, F., et al. 2016a, MNRAS, 460, 3587
—. 2016b, MNRAS, 460, 3587
Maseda, M. V., Bacon, R., Lam, D., et al. 2020, MNRAS, 493, 5120
Mawatari, K., Inoue, A. K., Hashimoto, T., et al. 2020, ApJ, 889, 137
McLeod, D. J., McLure, R. J., & Dunlop, J. S. 2016, MNRAS, 459, 3812
McLure, R. J., Dunlop, J. S., Cullen, F., et al. 2018, MNRAS, 476, 3991
Meurer, G. R., Heckman, T. M., & Calzetti, D. 1999, ApJ, 521, 64
Morishita, T., Trenti, M., Stiavelli, M., et al. 2018, ApJ, 867, 150
Neistein, E., & Dekel, A. 2008, MNRAS, 388, 1792
Oesch, P. A., Bouwens, R. J., Illingworth, G. D., Labbé, I., & Stefanon, M. 2018, ApJ, 855, 105
Oesch, P. A., Bouwens, R. J., Illingworth, G. D., et al. 2013, ApJ, 773, 75
—. 2014, ApJ, 786, 108
Oesch, P. A., Brammer, G., van Dokkum, P. G., et al. 2016, ApJ, 819, 129
Oke, J. B., & Gunn, J. E. 1983, ApJ, 266, 713
Park, J., Mesinger, A., Greig, B., & Gillet, N. 2019, MNRAS, 484, 933
Planck Collaboration, Aghanim, N., Akrami, Y., et al. 2020, A&A, 641, A6
Rasappu, N., Smit, R., Labbé, I., et al. 2016, MNRAS, 461, 3886
Roberts-Borsani, G., Morishita, T., Treu, T., Leethochawalit, N., & Trenti, M. 2022, ApJ, 927, 236
Roberts-Borsani, G. W., Ellis, R. S., & Laporte, N. 2020, MNRAS, 497, 3440
Roberts-Borsani, G. W., Bouwens, R. J., Oesch, P. A., et al. 2016, ApJ, 823, 143
Salmon, B., Papovich, C., Finkelstein, S. L., et al. 2015, ApJ, 799, 183
Salmon, B., Coe, D., Bradley, L., et al. 2018, ApJL, 864, L22
—. 2020, ApJ, 889, 189
Salpeter, E. E. 1955, ApJ, 121, 161
Santini, P., Fontana, A., Castellano, M., et al. 2017, ApJ, 847, 76
Schaerer, D., & de Barros, S. 2009, A&A, 502, 423
—. 2010, A&A, 515, A73
Smit, R., Bouwens, R. J., Labbé, I., et al. 2016, ApJ, 833, 254
—. 2014, ApJ, 784, 58
Song, M., Finkelstein, S. L., Ashby, M. L. N., et al. 2016, ApJ, 825, 5
Stark, D. P., Schenker, M. A., Ellis, R., et al. 2013, ApJ, 763, 129
Stark, D. P., Ellis, R. S., Charlot, S., et al. 2017, MNRAS, 464, 469
Stefanon, M., Bouwens, R. J., Illingworth, G. D., et al. 2022a, arXiv e-prints, arXiv:2204.02986
Stefanon, M., Bouwens, R. J., Labbé, I., et al. 2021a, ApJ, 922, 29

—. 2022b, ApJ, 927, 48
—. 2017, ApJ, 843, 36
Stefanon, M., Labbé, I., Bouwens, R. J., et al. 2019, ApJ, 883, 99
Stefanon, M., Labbé, I., Oesch, P. A., et al. 2021b, ApJS, 257, 68
Strait, V., Bradač, M., Coe, D., et al. 2020, ApJ, 888, 124
—. 2021, ApJ, 910, 135
Tacchella, S., Bose, S., Conroy, C., Eisenstein, D. J., & Johnson, B. D. 2018, ApJ, 868, 92
Tacchella, S., Finkelstein, S. L., Bagley, M., et al. 2022, ApJ, 927, 170
Topping, M. W., Stark, D. P., Endsley, R., et al. 2022, arXiv e-prints, arXiv:2203.07392
Walter, F., Decarli, R., Aravena, M., et al. 2016, ApJ, 833, 67
Weinmann, S. M., Neistein, E., & Dekel, A. 2011, MNRAS, 417, 2737
Wilkins, S. M., Bouwens, R. J., Oesch, P. A., et al. 2016a, MNRAS, 455, 659
Wilkins, S. M., Feng, Y., Di-Matteo, T., et al. 2016b, ArXiv e-prints, arXiv:1605.05044
Windhorst, R. A., Cohen, S. H., Hathi, N. P., et al. 2011, ApJS, 193, 27
Zheng, W., Postman, M., Zitrin, A., et al. 2012, Nature, 489, 406
Zheng, W., Zitrin, A., Infante, L., et al. 2017, ApJ, 836, 210
Zitrin, A., Labbé, I., Belli, S., et al. 2015, ApJL, 810, L12